Biomaterials 31 (2010) 9310–9319

Contents lists available at ScienceDirect

Biomaterials

journal homepage: www.elsevier.com/locate/biomaterials

Self-assembled fluorescent magnetic nanoprobes for multimode-biomedical imaging

Eun-Kyung Lim [a], Jaemoon Yang [b], Colin P.N. Dinney [c], Jin-Suck Suh [b], Yong-Min Huh [b,**], Seungjoo Haam [a,*]

[a] Department of Chemical and Biomolecular Engineering, College of Engineering, Yonsei University, Seoul 120-749, Republic of Korea
[b] Department of Radiology, College of Medicine, Yonsei University, Seoul 120-752, Republic of Korea
[c] Department of Urology, The University of Texas, M.D. Anderson Cancer Center, Houston, TX 77030, USA

ARTICLE INFO

Article history:
Received 29 June 2010
Accepted 21 July 2010
Available online 20 September 2010

Keywords:
Nanoprobe
Magnetic resonance imaging
Multimode
Fluorescent

ABSTRACT

We fabricated multimode nanoprobes for acquisition of biological information at different object levels, i.e., *in vivo* detection and *ex vivo* validation for characterizing tumor angiogenesis. Fluorescent magnetic nanoprobes (FMNPs) were synthesized by using amphiphilic pyrenyl polyethylene glycol (Py-PEG) and superparamagnetic $MnFe_2O_4$ nanocrystals (MNCs). Py-PEG, which is synthesized by conjugation of hydrophilic PEG with hydrophobic and fluorescent 1-pyrenebutyric acid through an esterification process, is capable of self-assembly and maintaining a high UV fluorescent intensity in aqueous phase. Py-PEG can be used as a fluorescent surfactant that simultaneously and efficiently encapsulates MNCs to exhibit fluorescent and magnetic properties as well as maintaining high water-solubility. Consequently, we proved that our biologically non-toxic FMNPs were prominent multimode imaging probes by showing not only excellent MR sensitivity but also high illumination intensity with strong signal strength under short exposure time of UV light from the extensive imaging studies of *in vitro/vivo* and *ex vivo* using orthotopic and xenograft mice models.

1. Introduction

Molecular nanoprobes using well-tailored superparamagnetic nanocrystals are of great interest for detecting various biological objects via magnetic resonance (MR) imaging due to their high-sensitivity and specificity gifted from a nanoeffect [1–4]. Further, the superparamagnetic nanocrystals as an MR contrast agent are hybridized with organic/inorganic fluorescent materials to create a single nanoplatform of multimodal imaging nanoprobes, which are utilized to measure *in vivo* biological events via MR and optical imaging at the same level of biological objects. In particular, both fluorescent and magnetic properties from conjugated multimodal imaging nanoprobes have been majorly used to render accurate appreciation of clinically significant events of cells, tissues and organisms via dual monitoring. Furthermore, a challenge for acquisition of biological information at different object levels, such as *in vivo* detection and *ex vivo* validation by using multimodal imaging methods to characterize tumor angiogenesis has been emerged [5–15]. Ultraviolet (UV) imaging has been recently introduced to provide higher spatial resolution with detailed insight into cellular events compared to visible light due to their shorter wavelength illumination. Thus, it would be of great significance to integrate MR imaging (*in vivo*) with UV imaging (*ex vivo*) for more robust acquisition of biological event with higher spatial resolution. However for UV imaging, to acquire high spatial intra-cellular resolution while keeping the cells alive and undamaged as long as possible, higher illumination intensities and longer exposure times over which cells are observed before they exhibit signs of damage should be necessary to provide sufficient signal strength [16–18]. Herein, we presented a fluorescent magnetic nanoprobe (FMNP) as a multimodal imaging agent. The fabrication of FMNP began with synthesizing pyrenyl polyethylene glycol (Py-PEG) with methoxy poly(ethylene glycol) (PEG) and 1-pyrenebutyric acid (Py) exhibiting amphiphilic and UV fluorescent properties. Then a simultaneous self-assembly of hydrophobic magnetic nanocrystals and Py-PEG as a fluorescent surfactant formed FMNPs utilized for UV and MR imaging capability (Fig. 1).

2. Materials and methods

2.1. Materials

The following materials were purchased from SigmaeAldrich: iron (III) acetylacetonate, 1,2-hexadecanediol, dodecanoic acid, dodecylamine, benzyl

* Corresponding author. Tel.: +82 2 2123 2751; fax: +82 2 312 6401.
** Corresponding author. Tel.: +82 2 2228 2375; fax: +82 2 362 8647.
E-mail addresses: ymhuh@yuhs.ac (Y.-M. Huh), haam@yonsei.ac.kr (S. Haam).

0142-9612/$ – see front matter
doi:10.1016/j.biomaterials.2010.07.081

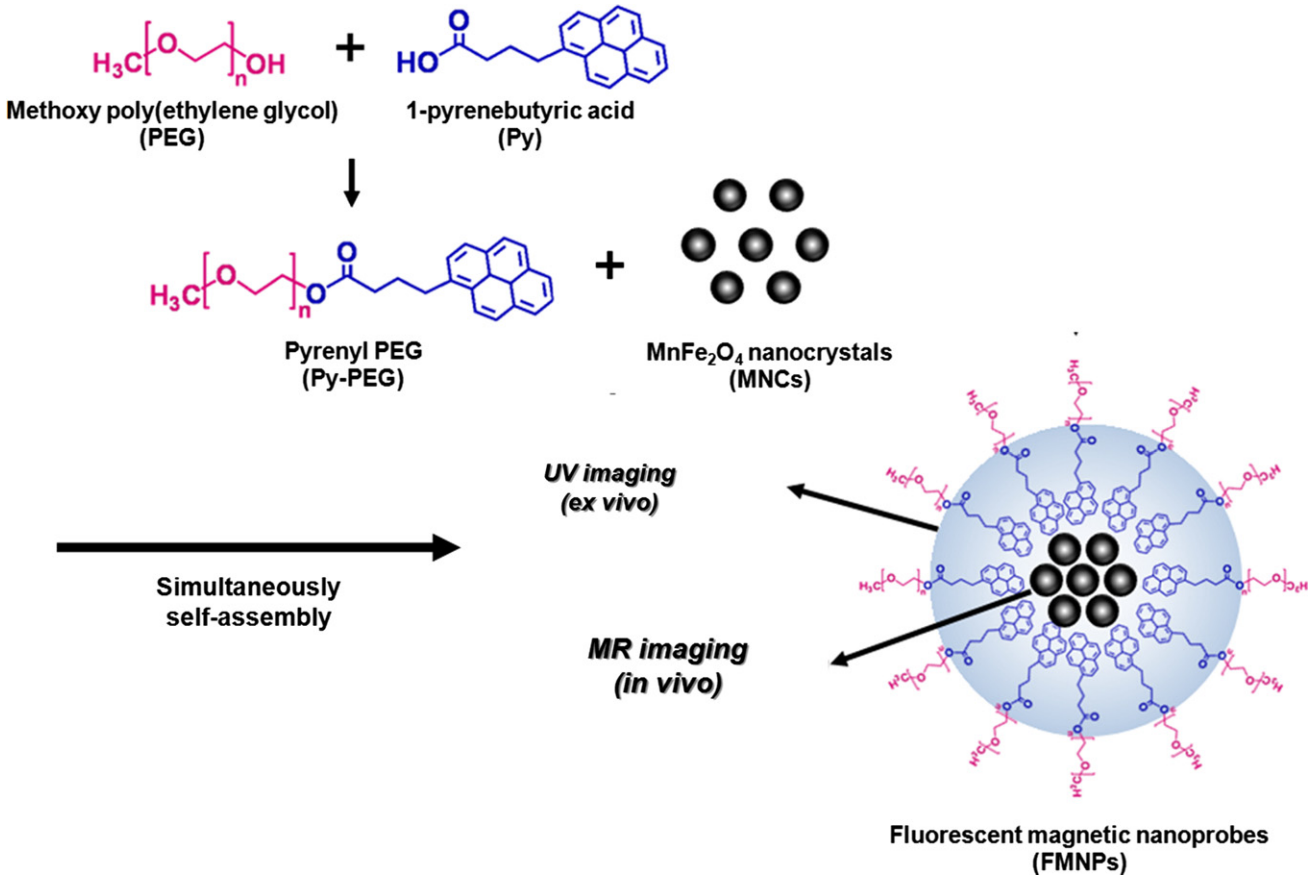

Fig. 1. Schematic illustration of simultaneously self-assembled fluorescent magnetic nanoprobes (FMNPs) as multimodal biomedical imaging probes.

ether, 1-pyrenebutyric acid, 1,3-dicyclohexylcarbodiimide (DCC), 4-dimethylaminopyridine (DMAP), anhydrous dichloromethane, and triethylamine (TEA). Monomethoxy polyethylene glycol (MW: 5000 Da) was obtained from Fluka Chemical Co. Phosphate buffered saline (PBS; 10 mM, pH 7.4) and DMEM were purchased from Gibco. All other chemicals and reagents were of analytical grade.

2.2. Synthesis of $MnFe_2O_4$ nanocrystals (MNCs)

Using a previously reported method, we synthesized monodispersed $MnFe_2O_4$ nanocrystals (MNCs) that are soluble in non-polar organic solvent [19–21]. Briefly, 2 mmol of iron (III) acetylacetonate, 1 mmol of manganese (II) acetylacetonate, 10 mmol of 1,2-hexadecanediol, 6 mmol of dodecanoic acid, and 6 mmol of dodecylamine were dissolved in 20 mL of benzyl ether under ambient nitrogen atmosphere. The mixture was then pre-heated to 200 °C for 2 h and refluxed at 300 °C for 30 min. After the reactants were cooled at room temperature, the products were purified with an excess of pure ethanol. Approximately 12 nm of MNCs were synthesized using the seed-mediated growth method.

2.3. Synthesis of pyrenyl polyethylene glycol (Py-PEG)

Pyrenyl polyethylene glycol (Py-PEG), an amphiphilic fluorescent surfactant, was formed by conjugating the hydroxyl group of monomethoxy polyethylene glycol (Mw: 5000 Da) with the carboxyl group of 1-pyrenebutyric acid (Mw: 288.34 Da) using DCC and DMAP (Fig. 1) [20,21]. First, 1 mmol of 1-pyrenebutyric acid and 1 mmol of monomethoxy polyethylene glycol were added into a flask containing 100 mL of anhydrous dichloromethane, 9 mmol of DCC, 9 mmol of DMAP, and 9 mmol of triethylamine (Sigma Aldrich Chemical). After reacting for 48 h at room temperature under a nitrogen atmosphere, the reactants were filtrated through a 200 nm pore size cellulose acetate filter (Advantec) to remove the by-product (dicyclohexyl urea). Subsequently, the solvent was rapidly removed using a rotary evaporator (50 Hz, EYELA) and the products were washed using dichloromethane and an excess of ethyl ether. The purified precipitates were lyophilized and stored under vacuum for later use.

2.4. Characterization of Py-PEG

The synthesis of Py-PEG was performed as follows (Fig. 1). After the conjugation process, the chemical structure of the synthesized Py-PEG was confirmed by FT-IR (Varian, ExcaliburTM series) and ^{1}H NMR (400 MHz, Varian INOVA400 NMR spectrometer) spectra using $CDCl_3$ as a solvent. In addition, the change in molecular weight of Py-PEG compared with naked PEG was evaluated by gel permeation chromatography analysis. Fluorescence intensities of Py-PEG compared with pyrene and critical micelle concentration (CMC) of Py-PEG were determined by fluorescence spectrometer readings (SL55, Perkin Elmer) [22,23].

2.5. Preparation of fluorescent magnetic nanoprobes (FMNPs)

FMNPs were prepared by the nano-emulsion method utilizing the hydrophobic interaction of MNCs with the hydrophobic portion of Py-PEG [9,24,25]. First, 50 mg of MNCs were dissolved in 4 mL of hexane (as organic phase). This organic phase was added to 20 mL of deionized water (DW) as an aqueous phase containing 200 mg of Py-PEG. After mutual saturation of the organic and water phases, the emulsion was ultra-sonicated in an ice-cooled bath for 10 min at 450 W. The resulting suspension was stirred overnight at room temperature to evaporate organic solvent and was subsequently centrifuged for 30 min at 18,000 rpm in triplicate. After the supernatant was removed, the precipitated FMNPs were re-dispersed in 10 mL of DW. The size distribution and the zeta-potential of FMNPs were analyzed using laser scattering (ELS-Z, Otsuka electronics). The morphologies of FMNPs and MNCs were confirmed using high resolution transmission electron microscope (HR-TEM, JEM-2100F, JEOL Ltd.). The colloidal stability of the prepared FMNPs was determined based on the resistance ability against the addition of a wide range of salt (sodium chloride, NaCl) solution concentrations (up to 1 M) and pH conditions (pH 4–9) at room temperature. After 24 h, the stability of the FMNPs was evaluated using laser scattering. The residual weight (%) of the MNCs in the FMNPs was analyzed with a thermo-gravimetric analyzer (SDT-Q600, TA instrument). We also confirmed the crystallinity of MNCs in the FMNPs using X-ray diffraction (Rigaku, X-ray Diffractometer Ultima3) at 298 K [2,4]. The magnetic properties of MNCs and FMNPs were measured using vibration sample magnetometer (MODEL-7300, Lakeshore) at 298 K. The relaxivity (R2) and fluorescence properties of the FMNP solution were measured by magnetic resonance (MR) imaging analysis and fluorescence

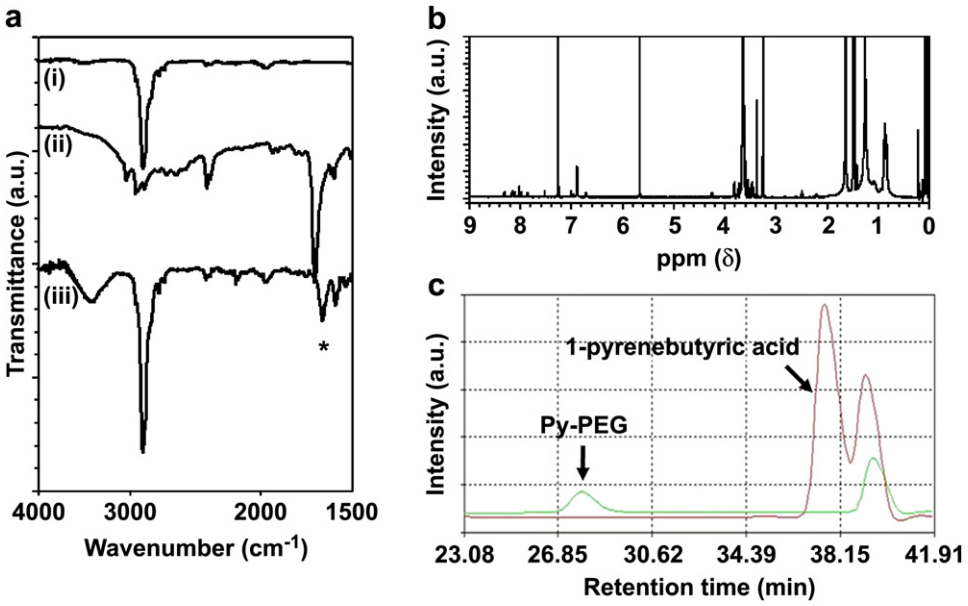

Fig. 2. (a) FT-IR spectra of (i) monomethoxy polyethylene glycol (mPEG), (ii) 1-pyrenebutyric acid and (iii) pyrenyl PEG (Py-PEG), (b) ^{1}H NMR spectrum of Py-PEG and (c) gel permeation chromatography of Py-PEG and 1-pyrenebutyriuc acid.

spectrometer, respectively. Furthermore, the magnetic mobility and ability to maintain fluorescent properties of the FMNPs were demonstrated under an external magnetic field (Nd–Fe–B magnet, 0.3 T).

2.6. In vitro cytotoxicity tests for Py-PEG and FMNPs

The cytotoxicity of Py-PEG and FMNPs in NIH3T6.7 cells (American Type Culture Collection) was evaluated by measuring the inhibition of cell growth using the MTT assay. Briefly, NIH3T6.7 cells were seeded at a density of 1×10^4 cells/well in a 96-well plate for growth overnight at 37 °C. Subsequently, the cells were incubated with various concentrations of Py-PEG and FMNPs for 24 h. The yellow tetrazolium salt of the MTT solution was reduced to purple formazan crystals in metabolically alive cells [25]. The cell viabilities were obtained by calculating the ratio of the intensity of purple formazan in viable cells treated with Py-PEG and FMNPs to the intensity in untreated control cells.

2.7. Cellular uptake of FMNPs

NIH3T6.7 cells (1×10^6 cells/well) were incubated overnight in 6-wells and were then further incubated with FMNPs (2.7 μg/mL) in 5% CO_2 for 24 h at 37 °C. Subsequently, NIH3T6.7 cells treated with FMNPs were washed twice with phosphate buffered solution (pH 7.4 and 10 mM), trypsinized (0.5 mL), and harvested. The collected NIH3T6.7 cells treated with FMNPs were washed in triplicate using 0.2% fetal bovine serum and 0.02% NaN_3 in phosphate buffered solution (pH 7.4 and 10 mM). NIH3T6.7 cells treated with FMNPs (1×10^6 cells/well) were then re-suspended in 200 μL of 4% paraformaldehyde for MR and UV light imaging analysis (UVIpro™ Gel Documentation System, Uvitec). To locate the nucleus in cells through florescence microscopic images, cells were stained by propidium iodide (red fluorescence) (16.7 μg/mL) [9]. The cellular internalization of FMNPs was confirmed by Prussian blue staining, epi-fluorescence microscopy (BX51 upright microscope, Olympus), and transmission electron microscopy (TEM, JEOL-1100). The concentration of MNCs (Mn and Fe ions) in NIH3T6.7 cells treated with FMNPs was determined by inductively coupled plasma mass spectrometry (ICP-MS, Elan 6100, Perkin Elmer). The magnetic and optical properties of NIH3T6.7 cells treated with FMNPs were demonstrated under an external magnetic field (Nd–Fe–B magnet, 0.3 T).

2.8. Animal experimental procedure

For investigation of tumor imaging, we established orthotopic tumor model, to which 253JB-V bladder tumor cell lines (7×10^5 cells per mouse) were implanted into the bladder dome of a male mouse (~6-week-old BALB/c-nude mice) and then MR imaging was performed between 4 and 6 weeks after tumor cell implantation [26]. Furthermore, we performed xenograft tumor model that NIH3T6.7 cells (1×10^7 cells suspended in 50 μL of saline per animal) were implanted in the proximal thigh of female BALB/c-nude mice (4–5 weeks of age) [21,27]. All animal

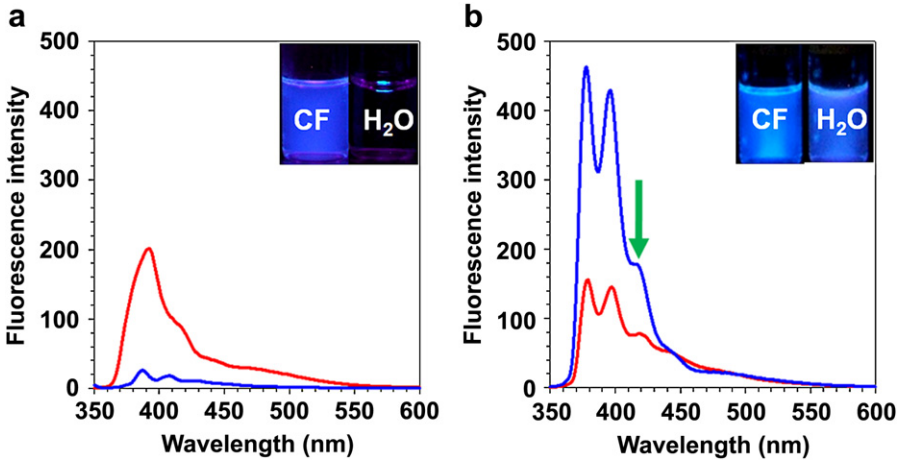

Fig. 3. Fluorescence spectra and solubility tests under UV lamp (inset) of pyrene and (b) Py-PEG in chloroform (CF, red line) and water (H_2O, blue line) (λ_{ex}: 340 nm). The green arrow indicates an excimer of Py-PEG.

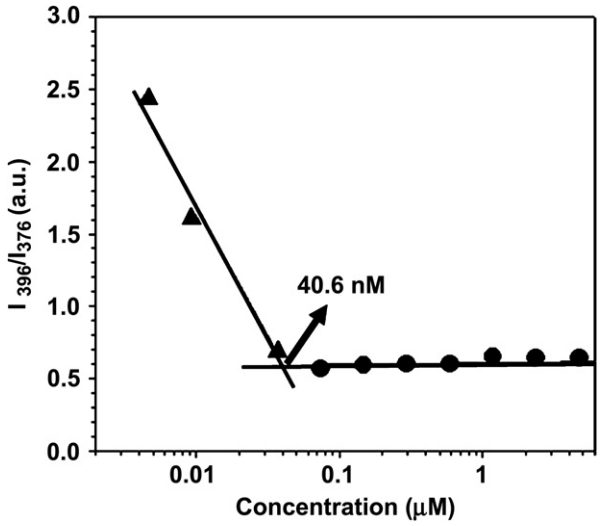

Fig. 4. The fluorescent intensity ratio (I_{396}/I_{376}) from the pyrenyl group excitation spectra with different concentrations of Py-PEG (λ_{ex}: 340 nm).

experiments were conducted with the approval of the Association for Assessment and Accreditation of Laboratory Animal Care (AAALAC) International.

2.9. MR imaging procedure

We performed *in vitro* MR imaging experiments with a 1.5 T clinical MRI instrument with a micro-47 surface coil (Intera; Philips Medical Systems, Best, the Netherlands). The T2 weights of the FMNP solution and FMNPs treated NIH3T6.7 cells treated were measured by the Carr-Purcell-Meiboom-Gill (CPMG) sequence at room temperature: TR = 10 s, 32 echoes with 12 ms even echo space, number of acquisition = 1, point resolution of 156 × 156 μm, section thickness of 0.6 mm. For acquisition of T2-weighted MR images of FMNPs and FMNPs treated NIH3T6.7 cells, the following parameters were adopted: resolution of 234 × 234 μm, section thickness of 2.0 mm, TE = 60 ms, TR = 4000 ms, number of acquisitions = 1. The relaxivity coefficient (m_M^{-1} s^{-1}) is equal to the ratio of R2 (1/T2, s^{-1}) to FMNP concentration. In addition, *In vivo* MR imaging experiments were also performed with a 3 T clinical MRI instrument with a micro-47 surface coil (Intera; Philips Medical Systems, Best, the Netherlands). The T2 weights of nude mouse injected with FMNPs were measured by the Carr-Purcell-Meiboom-Gill (CPMG) sequence at room temperature: TR = 10 s, 32 echoes with 12 ms even echo space, number of acquisition = 1, point resolution of 156 × 156 μm, section thickness of 0.6 mm. For T2-weighted MR imaging of nude mouse model, we adopted the following parameters: resolution of 234 × 234 μm, section thickness of 2.0 mm, TE = 60 ms, TR = 4000 ms, number of acquisitions = 1.

2.10. Statistical analysis

All data represent triplicate experiments, with each experiment yielding comparable results. The statistical evaluation of data was performed by the analysis of variance (Student's *t*-test). A *p*-value of less than 0.001 was considered statistically significant.

3. Results and discussion

Monodispersed $MnFe_2O_4$ nanocrystals (MNCs) were synthesized as MR contrast agents by the thermal decomposition method. For phase transference of MNCs into aqueous phase and implementation of their fluorescent property at once, we synthesized a pyrenyl polyethylene glycol (Py-PEG) as a fluorescent surfactant by coupling of 1-pyrenebutyric acid and PEG by an esterification process. DCC was used to prepare active carboxylate from 1-pyrenebutyric acid. Then, the prepared carboxylate was coupled with DMAP as the nucleophilic catalyst through the labile ion pair between the carboxylate and the acetylpyridinium ions. Finally, the hydroxyl group of PEG, serving as a nucleophile, attacked the low electric carbon of the acetyl group to form an ester bond, and a protonated catalyst was reformed. Thus, the generated ester group of Py-PEG was confirmed at 1737 cm^{-1} and the hydroxyl group of PEG and carboxyl group of 1-pyrenebutyric acid were no longer observed at 3500 cm^{-1} and 1695 cm^{-1}, respectively (Fig. 2a). Moreover, successful synthesis of Py-PEG was further verified by its ^1H NMR spectrum at 7.82 and 8.12 (−CH− from 1-pyrenebutyric acid) and 3.65 ppm ($-CH_2-$ in the PEG chain) (Fig. 2b). In addition, the incremental change in molecular weight of Py-PEG from 5000 Da (naked PEG) to 5288 Da was evaluated by gel permeation chromatography analysis (Fig. 2c). Naked pyrene is insoluble in water due to the non-polar and hydrophobic properties of its four symmetric fused benzene rings. However, PEGylated pyrene (Py-PEG) can be highly soluble in water because of its hydrophilic property resulting from hydrogen bonding between the oxygen atoms of PEG and water molecules (Fig. 3) [28]. Due to the amphiphilic property of Py-PEG, the hydrophobic pyrenyl group of Py-PEG is surrounded by hydrophilic PEG chains. As the Py-PEG concentration increased, the fluorescence intensity ratio of Py-PEG (I_{396}/I_{376}) spontaneously declined and the critical micelle concentration was 40.6 nm (Fig. 4). In addition, the pyrene molecules of Py-PEG maintained a high electron density compared to the naked pyrene molecules and exhibited strong excited-state dimers (excimer) because of the closely packed pyrene units in the Py-PEG micelle (Fig. 3). The synthesized Py-PEG exhibited a high fluorescent intensity at 375 and 398 nm and strong excimer at 420 nm due to interactions between the excited pyrene molecules of Py-PEG and another pyrene molecule in the ground electronic state, promoted by the high electron density of pyrene molecules [29]. These results indicate that the synthesized Py-PEG successfully played a role of amphiphilic fluorescent surfactant for

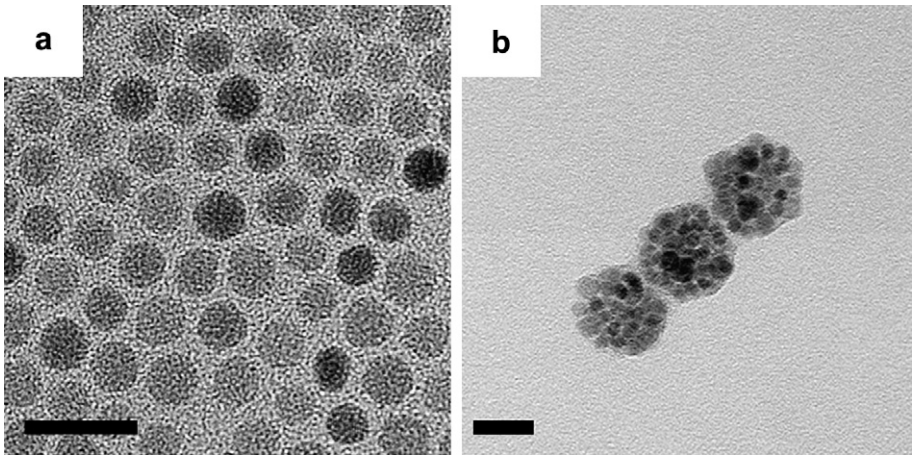

Fig. 5. TEM images of (a) $MnFe_2O_4$ nanocrystals (MNCs) and (b) fluorescent magnetic nanoprobes (FMNPs) (Scale bar: 20 nm).

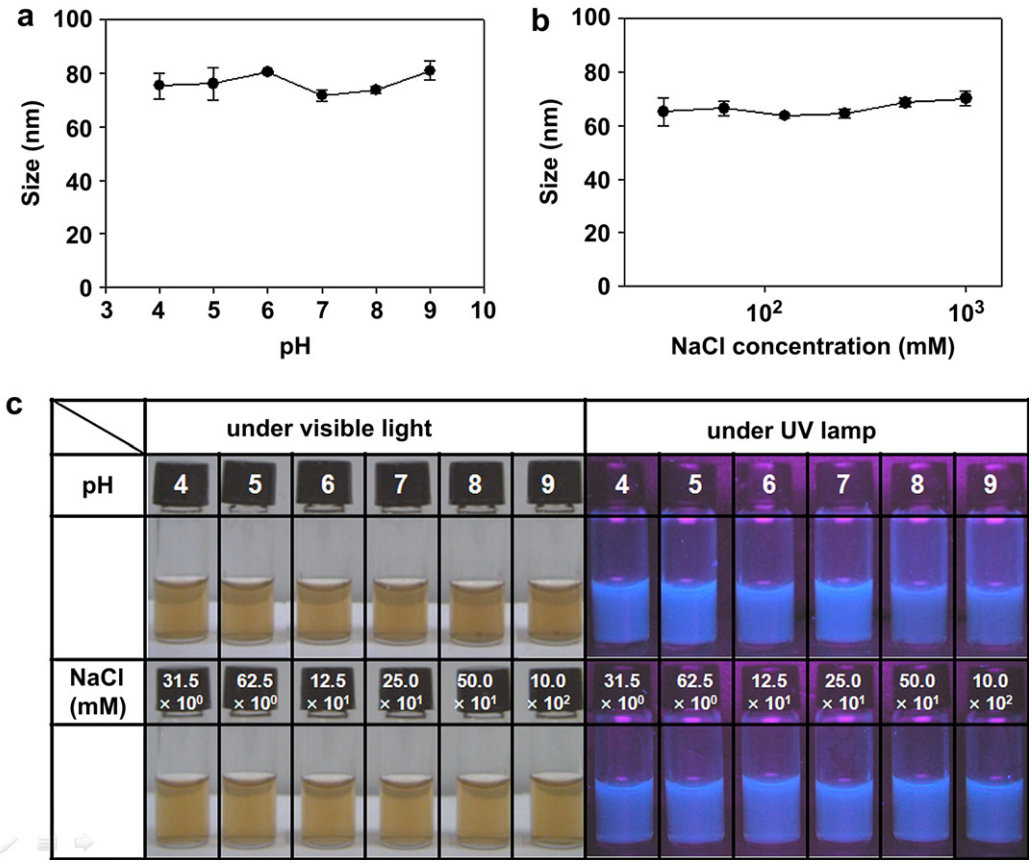

Fig. 6. The sizes of FMNPs were plotted against (a) pH conditions and (b) NaCl concentrations (mM) and (c) images of FMNPs under various pH conditions and NaCl concentrations (under visible light and UV light).

fabrication of FMNPs. To synthesize water-soluble FMNPs, hydrophobic MNCs were encapsulated by the amphiphilic fluorescent surfactant, Py-PEG, using a nano-emulsion method. MNCs in organic solvent were simultaneously wrapped by the self-assembly of Py-PEG molecules and water-soluble FMNPs were subsequently formulated by evaporation of the organic phase during the nano-emulsion process. Transmission electron microscopy (TEM) (Fig. 5b) and laser scattering analysis indicated complete dispersion of FMNPs in water with a consistent size distribution (64.1 ± 3.1 nm), which was similar to the observed dispersion of FMNPs in biological medium (10% fetal bovine serum and 1% penicillin streptomycin in DMEM) (69.8 ± 2.1 nm). FMNPs enveloped by non-ionic PEG molecules exhibited −0.4 ± 0.6 mV in water and −1.5 ± 0.3 mV in biological medium. In addition, FMNPs (533.5×10^{-2} mg/mL) were stable in a wide range of salt solutions (up to 1 M) and pH conditions (pH 4–9) without any aggregations (Fig. 6). While thermogravity analysis demonstrated that the organic compounds in FMNPs were 50 wt%, the mixed spinel structure of the MNCs was still maintained (2θ: 30.3° (220), 35.8° (311), 43.6° (400), 53.7° (422), 57.5° (511), and 62.7° (440)) (Fig. 7). Furthermore, FMNPs exhibited superparamagnetic behavior at 298 K without remanence and coercivity and the saturation of magnetization at 0.8 T of FMNPs was 41.9 emu/g of MNCs, which was similar to that for naked MNCs (43.2 emu/g of MNCs) (Fig. 8). To evaluate the potential use of FMNPs as

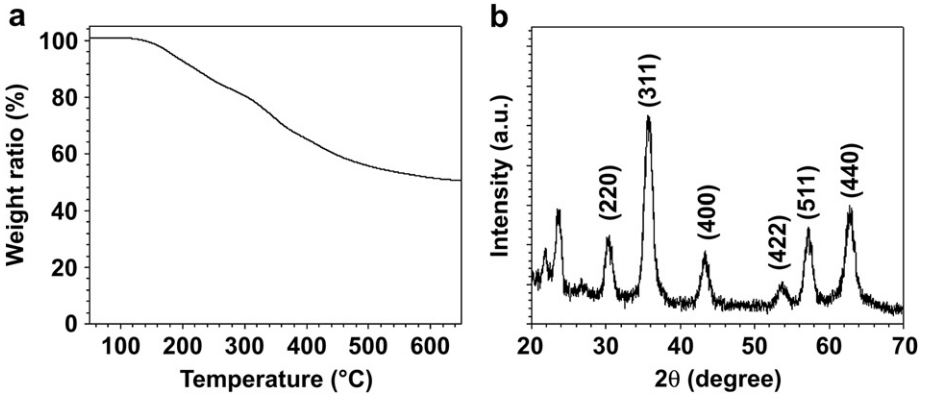

Fig. 7. (a) Thermogravity analysis and (b) X-ray diffraction (XRD) pattern of FMNPs with inserted main crystalline phases of MNCs.

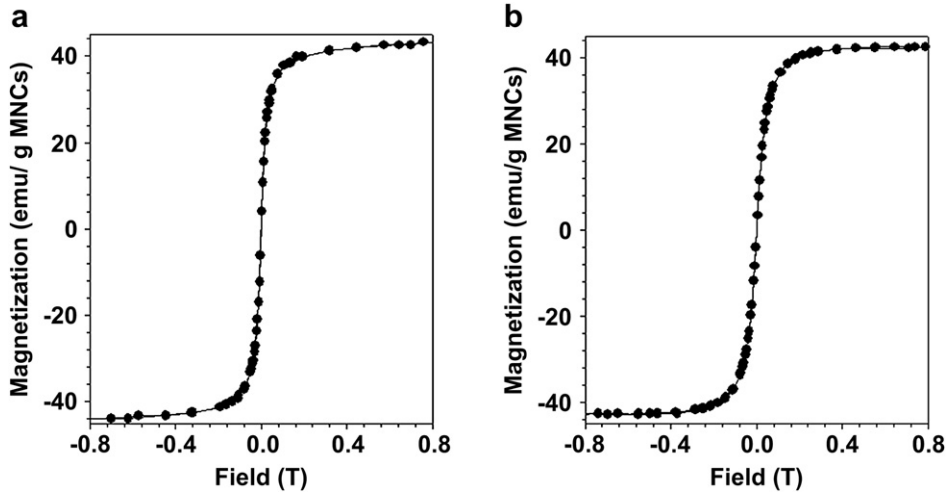

Fig. 8. Magnetic hysteresis loops of (a) MNCs and (b) FMNPs.

ultrasensitive MR imaging contrast agents, we investigated MR images of the FMNP solution and the signal intensities. T2-weighted MR images exhibited strong black color for the thicker FMNP solution and the corresponding relaxivity coefficient of FMNPs containing MNCs was 786.4 $mM^{-1}\,s^{-1}$ indicating that the FMNP solution has sufficient high-sensitivity for use as an MR imaging contrast agent (Fig. 9). To confirm the utility of FMNPs as optical imaging agents, we also investigated the fluorescence properties of FMNPs (λ_{ex}: 345 nm and λ_{em}: 397 nm). The fluorescence spectra of FMNPs are similar to those of Py-PEG, and even after loading MNCs into FMNPs the fluorescent peak from excimer at 420 nm was maintained (Fig. 10). Furthermore, water-soluble FMNPs exhibit vivid luminescent light under UV lamp (λ_{ex}: 365 nm) (Fig. 10, inset) and FMNPs are magnetically gathered by an external magnetic field (Nd–B–Fe magnet, 0.3 T), maintaining the fluorescent properties of the pyrene in the FMNPs (Fig. 11 and Movie 1). These excellent magnetic and optical properties of FMNPs provide abundant possibilities for multimodal-biomedical imaging.

Supplementary video related to this article can be found at doi:10.1016/j.biomaterials.2010.07.081.

To examine the cellular cytotoxicity of FMNPs, an MTT assay was performed using NIH3T6.7 cells treated with FMNPs. FMNPs exhibited biocompatibility without any inhibitory effect on growth and proliferation in the target NIH3T6.7 cells, even at a high concentration of 1.6 mg/mL (Fig. 12).

For assessment of the optical imaging performance of FMNPs, NIH3T6.7 cells were incubated with the non-cytotoxic FMNPs (21.3 μg/mL) and then visualized under UV light. In Fig. 13a, the fluorescent microscopic images of NIH3T6.7 cells treated with FMNPs revealed vivid fluorescent blue light in the cytosol due to fluid endocytosis of FMNPs, whereas there was no fluorescent blue staining in untreated cells (control) [9]. The red fluorescence in Fig. 13a represents nuclear site staining by Lyso tracker (10 nm). Due to the presence of pyrene from FMNPs, NIH3T6.7 cells treated with FMNPs also demonstrated a distinct luminescent light under

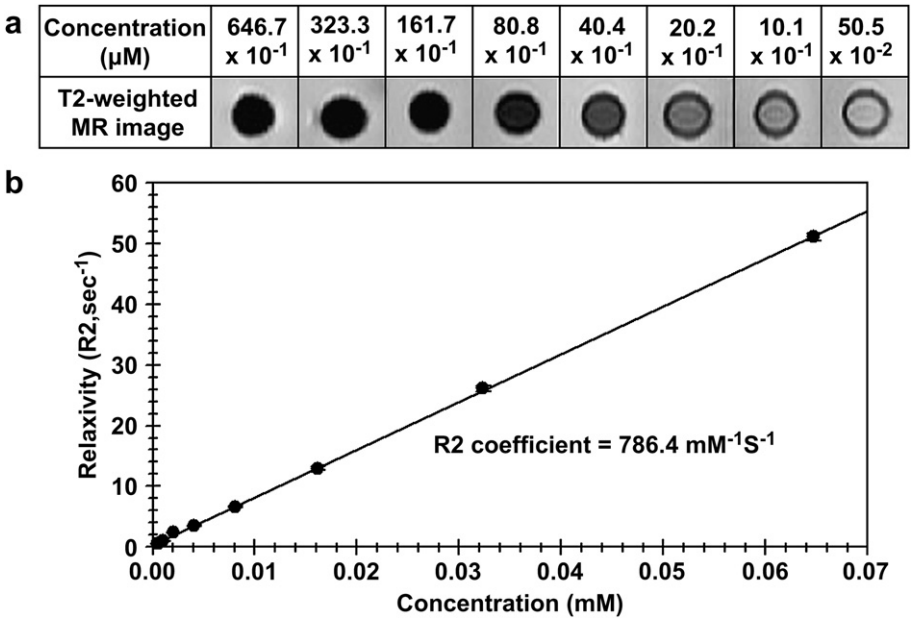

Fig. 9. (a) T2-weighted MR images and (b) relaxivity (R2) graph of FMNPs versus various concentrations.

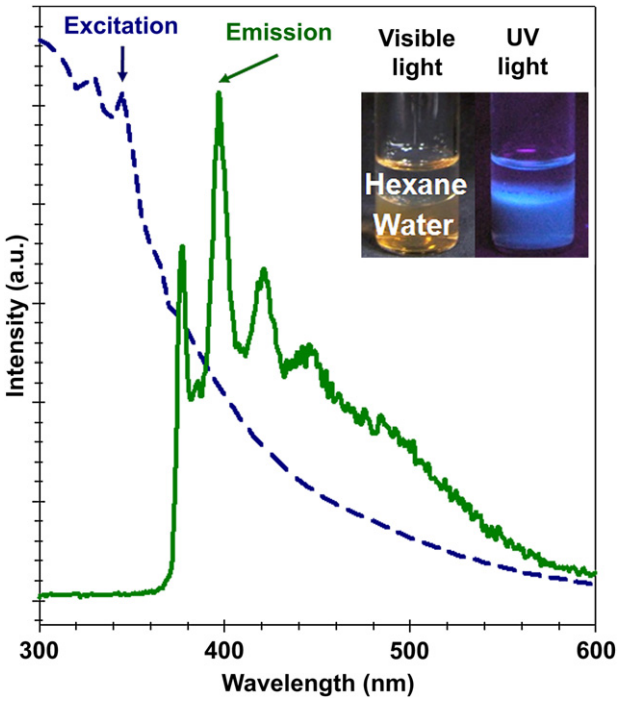

Fig. 10. Fluorescence spectra for FMNPs and solubility tests of FMNPs (insets) in aqeous phase under visible light and UV light (λ_{ex}: 340 nm).

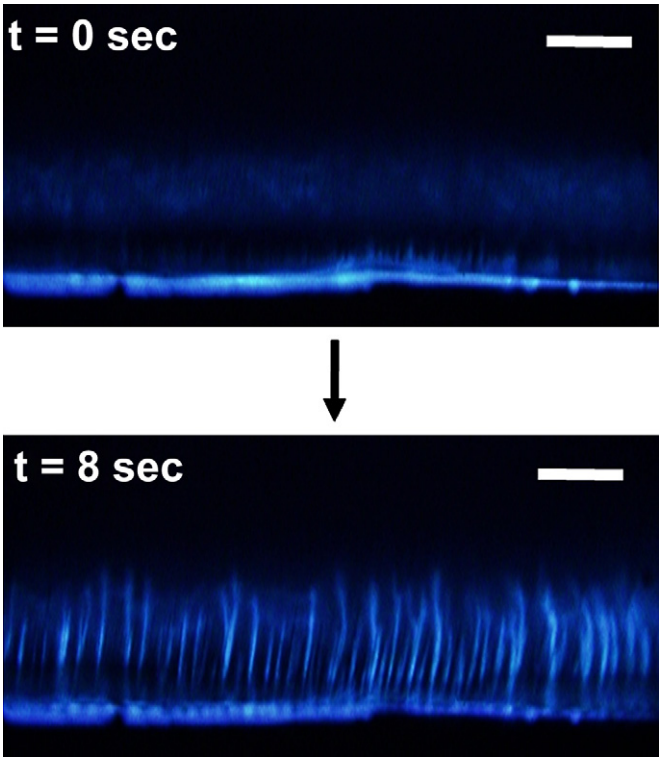

Fig. 11. Fluorescence microscopic images (×200) of colloidal FMNPs under magnetic field. Nd–Fe–B magnet (0.3 T) is applied at the lower portion of the image. FMNPs moved downward within 8 s (Scale bar = 100 μm).

UV lamp (λ_{ex}: 365 nm) compared with untreated control cells (subset in Fig. 13a). The results from Prussian blue staining and TEM images are consistent with the optical imaging results. We next investigated the MR contrast effect of FMNPs in NIH3T6.7 cells monitored at 1.5 T. A significant MR contrast effect was observed in treated cells (black color) compared to non-treated control cells (bright gray color) (subset in Fig. 13a). The calculated R2 value of NIH3T6.7 cells treated with FMNPs was 14.5 s^{-1}, which was 387.6% ($\triangle R2/R2_{Non\text{-}treatment}$) higher than that of non-treated cells (2.9 s^{-1}) (Fig. 13b). Prussian blue and ferric ions of the MNCs in FMNPs rapidly exchange electrons thereby producing dark blue colors in the intra-cellular region (subset in Fig. 13a). In the TEM images, the black clusters of NIH3T6.7 cells treated with FMNPs indicate the engulfment of FMNPs into the intra-cellular region (Fig. 13c). The concentration of MNCs (Mn and Fe ions) in NIH3T6.7 cells treated with FMNPs was 9.1 μg/mL (3.0×10^5 cells) measured by inductively coupled plasma mass spectrometry (ICP-MS) analysis. Furthermore, the well-dispersed NIH3T6.7 cells treated with FMNPs were sensitively and rapidly moved toward a permanent magnet exhibiting an intense luminescence under an external magnetic field (Nd–B–Fe magnet, 0.3 T) (Fig. 13d–e and Movie 2). These results demonstrate that FMNPs are suitable for use as molecular nanoprobes for highly versatile imaging and ultrasensitive detection at the cellular level.

Supplementary videos related to this article can be found at doi:10.1016/j.biomaterials.2010.07.081.

We next performed MR imaging of xenograft mice models using FMNPs as an MR contrast agent for passive cancer detection. First, nude mice were subcutaneously implanted in the proximal thigh with NIH3T6.7 cells to develop xenograft mouse model. Magnetic resonance (MR) images were then obtained before and after intravenous injection of FMNPs (300 μg Fe + Mn in FMNPs), respectively. After the injection of FMNPs (post-injection), the T2 value was immediately dropped at tumor site (increase in $\triangle R2/R2_{Pre}$ value; $\triangle R2 = R2 - R2_{Pre}$) and strong MR signal intensity was observed compared to pre-contrast images. In T2-weighted MR images, the black color gradually spread out along change of the T2 value ($R2 = 1/T2$; $\triangle R2/R2_{Pre}$: 64.16%), following the peripheral blood vessel of tumor area because the FMNPs were diffused and permeated to tumor tissues across corresponding vascular distributions due to enhanced permeation and retention (EPR) effect (Fig. 14a and b) [2,21]. Furthermore, we performed *ex vivo* MR imaging of tumor tissue which explanted from a xenograft model treated with FMNPs, presented partially black color compared with non-treated tumor tissue. The MR image of tumor tissue exhibited

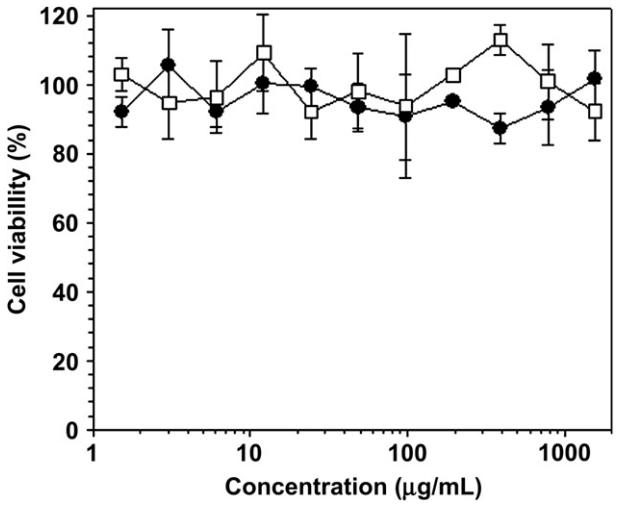

Fig. 12. Cell viabilities of NIH3T6.7 cells treated with various concentrations of Py-PEG (open square) and FMNPs (closed circle).

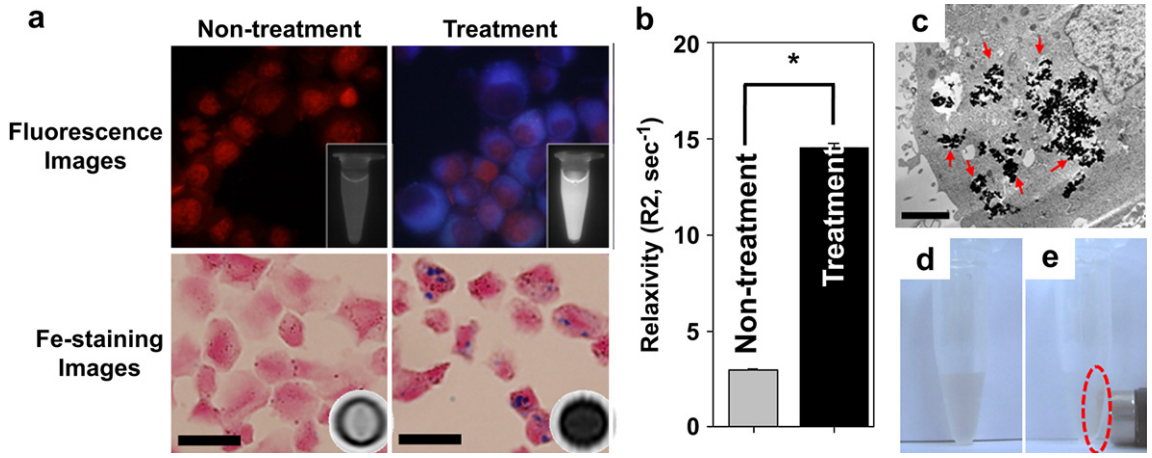

Fig. 13. (a) Fluorescence and Prussian blue stained microscopic images of NIH3T6.7 cells treated with and without FMNPs (upper insets: cellular images under UV light and lower insets: T2-weighted MR images of NIH3T6.7 cells) (Scale bar = 25 μm), (b) R2 graph for NIH3T6.7 cells treated with and without FMNPs (*$p < 0.001$), (c) the red arrows of TEM image indicates the existence of FMNPs in NIH3T6.7 cells (Scale bar = 2 μm) and magnetic mobilization of NIH3T6.7 cells treated with FMNPs dispersed in PBS in a microtube (d) without a magnetic field and (e) with a magnetic field (dashed red circles: drawn cells). The Nd–Fe–B magnet (0.3 T) is located at the right-side of the microtube.

the existence of fairly high amount of FMNPs ($\triangle R2/R2_{Non\text{-}treatment}$: 90.27%) due to blood pool effect and/or EPR effect of the tumor site (Fig. 14c and d). These results indicate promising potential application of FMNPs to detect the tumor as MR contrast agent. On the other hand, we next determined whether FMNPs are capable of detecting intratumoral tissue architecture which requires high resolution of cellular level via fluorescent microscopy at UV spectral bands. We analyzed the frozen *ex vivo* samples of tumor and muscle by using fluorescence microscopy. We observed vivid fluorescent blue and dark blue color dots in the interior of tumor tissue treated FMNPs, also confirmed MNCs of FMNPs were co-existence with fluorescenct properties through the Prussian blue staining images (Fig. 15). These results indicated that blue dots in *ex vivo* tumor tissue successfully confirmed the presence of FMNPs at microscopic resolution which was shown at *in vivo* MR images. In addition, we verified the passive tumor tissue detection capability of FMNPs as universal bimodal imaging nanoprobes by using blood pooling and/or EPR effect. Orthotopic bladder cancer mouse model was used in this experiment because it is more physiologically mimicking human cancer compared to xenograft one in terms of tumor

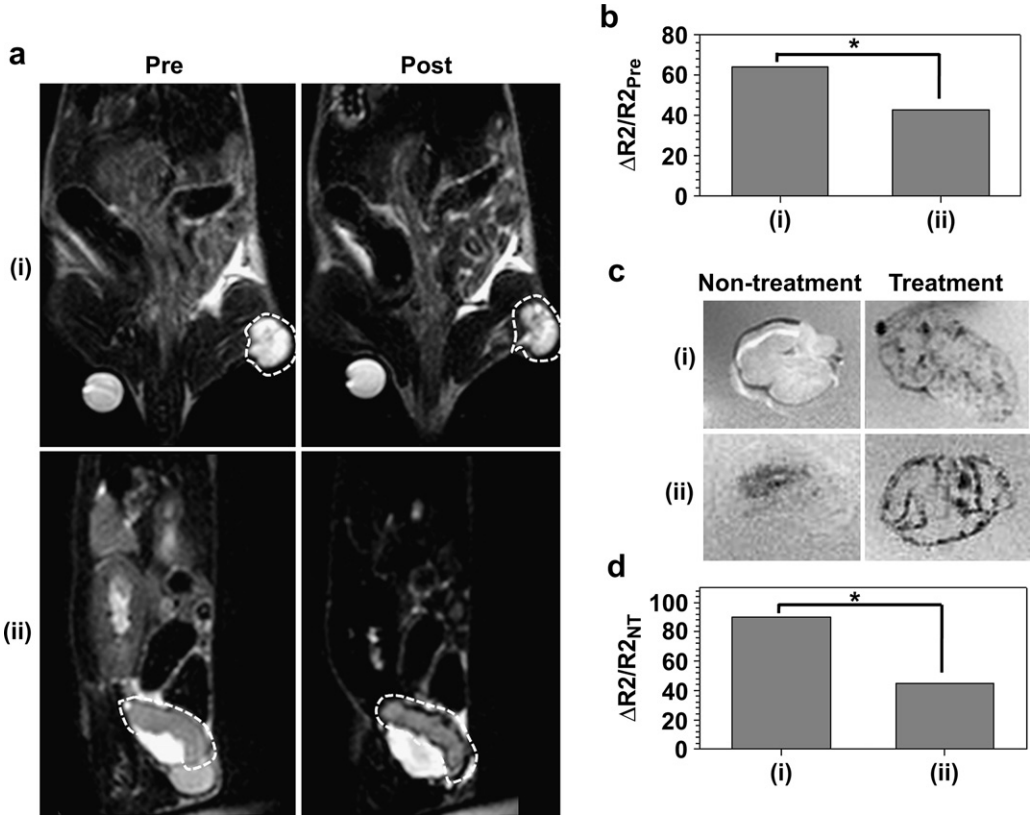

Fig. 14. (a) T2 – weighted MR images of xenografted model with NIH3T6.7 cells at proximal thigh region of mouse and orthotopic model with 253JB-V cells at bladder after injection of the FMNPs, (b) $\triangle R2/R2_{Pre}$ graph versus time pre-injection and post- injection of FMNPs, (c) *ex vivo* T2 – weighted MR images and (d) $\triangle R2/R2_{Non\text{-}treatment}$ graph of xenografted and orthotopic mouse treated with (treatment: T) and without FMNPs (non-treatement: NT), respectively (i: xenografted model and ii: orthotopic model) (*$p < 0.001$).

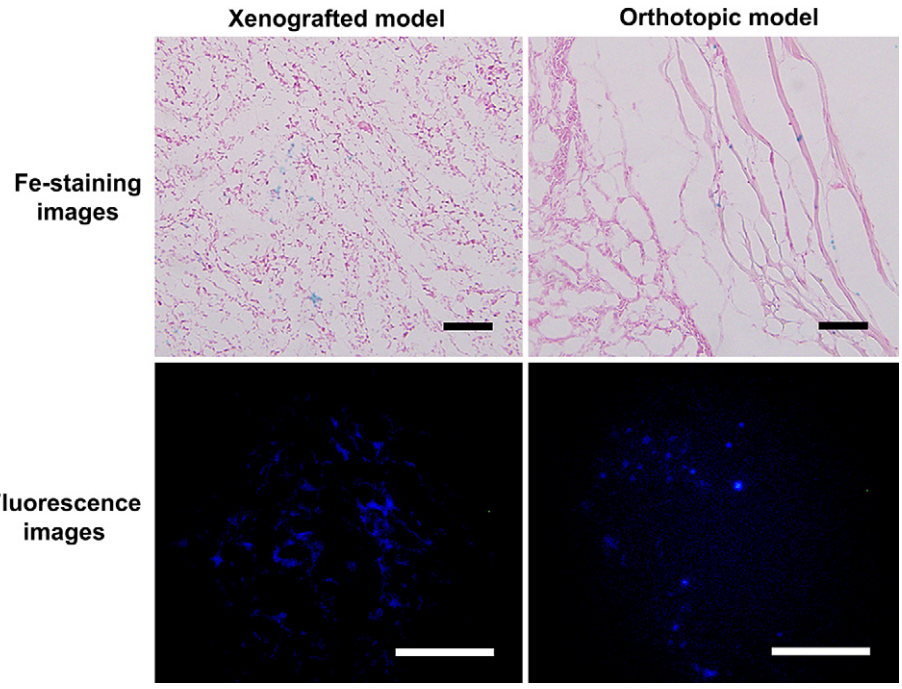

Fig. 15. Fe-staining and Fluorescence images of tissue slides of xenografted and orthotopic mouse treated with FMNPs, respectively (Scale bar = 20 μm).

neoangiogenesis based on "seed and soil" theory [30–32]. Interestingly, we observed an immediate decrease of the T2 value ($\triangle R2/R2_{Pre}$: 42.93%), following the central blood vessel of tumor site after FMNPs were spread out and permeated to tumor tissues by EPR effect (Fig. 14a and b) [21]. In addition, *ex vivo* MR imaging of tumor tissue from orthotopic model treated with FMNPs cross checked the evidence of existence of FMNPs in comparison to the untreated model as well ($\triangle R2/R2_{Non\text{-}treatment}$: 44.91%). These findings indicated that FMNPs demonstrated similar high performance imaging capability in orthotopic mouse model as well as xenograft mouse model (Figs. 14 and 15).

4. Conclusions

We introduce a facile and efficient strategy to fabricate FMNPs for universal nanoprobes to cover *ex vivo* high resolution modality at the cellular level as well as that of *in vivo* MRI. Py-PEG can be used as a fluorescent surfactant that simultaneously and efficiently encapsulates MNCs to induce fluorescent and magnetic properties as well as water-solubility. From the complete *in vitro/vivo* studies as well as *ex vivo* ones by using both orthotopic and xenograft mice models, FMNPs showed not only excellent sensitivity and feasibility as MR probes but also high illumination intensities and strong signal strength for short exposure times as UV imaging probes as well as exhibiting sufficient biocompatibility. Apart from the currently developed multimodal nanoprobes, it may be interesting to speculate the undiscovered merits of UV fluorescence/MRI multimode nanoprobes for better spatial resolution to obtain detailed biological information. Moreover, since a variety of hydrophobic fluorescent dyes and drugs can be easily assembled with hydrophobic core, this study may be extended to synthesize versatile nanocomplexes for imaging probes, drug delivery and cell separation.

Acknowledgments

This study was supported by a grant of the Korea Health 21 R&D Project, Ministry of Health & Welfare, Republic of Korea (A085136) and the National Research Foundation of Korea (NRF) funded by the Ministry of Education, Science and Technology (No. 2009-0084190).

Appendix

Figures with essential colour discrimination. Several of the figures in this article have parts that are difficult to interpret in black and white. The full colour images can be found in the on-line version, at doi:10.1016/j.biomaterials.2010.07.081.

References

[1] Weissleder R, Pittet MJ. Imaging in the era of molecular oncology. Nature 2008;452:580–9.
[2] Lee J-H, Huh Y-M, Jun Y-W, Seo J-W, Jang J-T, Song H-T, et al. Artificially engineered magnetic nanoparticles for ultra-sensitive molecular imaging. Nat Med 2007;13:95–9.
[3] Huh Y-M, Jun Y-W, Song H-T, Kim S, Choi J-S, Lee J-H, et al. In vivo magnetic resonance detection of cancer by using multifunctional magnetic nanocrystals. J Am Chem Soc 2005;127:12387–91.
[4] Jun Y-W, Huh Y-M, Choi J-S, Lee J-H, Song H-T, Cheon J, et al. Nanoscale size effect of magnetic nanocrystals and their utilization for cancer diagnosis via magnetic resonance imaging. J Am Chem Soc 2005;127:5732–3.
[5] Bertorelle F, Wilhelm C, Roger J, Gazeau F, Manager C, Cabuil V. Fluorescence-modified superparamagnetic nanoparticles: intracellular uptake and use in cellular imaging. Langmuir 2006;22:5385–91.
[6] Lee J-H, Jun Y-W, Yeon S-I, Shin J-S, Cheon J. Dual-mode nanoparticle probes for high-performance magnetic resonance and fluorescence imaging of neuroblastoma. Angew Chem Int Ed 2006;45:8160–2.
[7] Tsai C-P, Hung Y, Chou Y-H, Huang D-M, Hsiao J-K, Chang C, et al. High-contrast paramagnetic fluorescent mesoporous silica nanorods as a multifunctional cell-imaging probe. Small 2008;4:186–91.
[8] Yang J, Lee J, Kang J, Chung C-H, Lee K, Suh J-S, et al. Magnetic sensitivity enhanced novel fluorescent magnetic silica nanoparticles for biomedical applications. Nanotechnology 2008;19:075610–5.
[9] Yang J, Lim E-K, Lee HJ, Park J, Lee SC, Lee K, et al. Fluorescent magnetic nanohybrids as multimodal imaging agents for human epithelial cancer detection. Biomaterials 2008;29:2548–55.
[10] Seo S-B, Yang J, Lee E-S, Jung Y, Kim K, Lee S-Y, et al. Nanohybrids via a polycation-based nanoemulsion method for dual-mode detection of human mesenchymal stem cells. J Mater Chem 2008;18:4353–484.
[11] Kim J, Lee JE, Lee J, Yu JH, Kim BC, An K, et al. Magnetic fluorescent delivery vehicle using uniform mesoporous silica spheres embedded with monodisperse magnetic and semiconductor nanocrystals. J Am Chem Soc 2005;128:688–9.

[12] Medarova Z, Pham W, Kim Y, Dai G, Moore A. In vivo imaging of tumor response to therapy using a dual-modality imaging strategy. Int J Cancer 2006;118:2796–802.
[13] Josephson L, Kircher MF, Mahmood U, Tang Y, Weissleder R. Near-infrared fluorescent nanoparticles as combined MR/optical imaging probes. Bioconjug Chem 2002;13:554–60.
[14] Vuu K, Xie J, McDonald MA, Bernardo M, Hunter F, Zhang Y, et al. Gadolinium–rhodamine nanoparticles for cell labeling and tracking via magnetic resonance and optical imaging. Bioconjug Chem 2005;16:995–9.
[15] Talanov VS, Regino CAS, Kobayashi H, Bernardo M, Choyke PL, Brechbiel MW. Dendrimer-based nanoprobe for dual modality magnetic resonance and fluorescence imaging. Nano Lett 2006;6:1459–63.
[16] Parpura V, Tong W, Yeung ES, Haydon PG. Laser-induced native fluorescence (LINF) imaging of serotonin depletion in depolarized neurons. J Neurosci Methods 1998;82:151–8.
[17] Lillard SJ, Yeung ES. Temporal and spatial monitoring of exocytosis with native fluorescence imaging microscopy. J Neurosci Meth 1997;75:103–9.
[18] Lillard SJ, Yeung ES, McCloskey MA. Monitoring exocytosis and release from individual mast cells by capillary electrophoresis with laser-induced native fluorescence detection. Anal Chem 1996;68:2897–904.
[19] Sun S, Zeng H, Robinson DB, Raoux S, Rice PM, Wang SX, et al. Monodisperse MFe_2O_4 (M = Fe, Co, Mn). Nanoparticles J Am Chem Soc 2003;126:273–9.
[20] Lim E-K, Yang J, Park M-Y, Park J, Suh J-S, Yoon H-G, et al. Synthesis of water soluble PEGylated magnetic complexes using mPEG-fatty acid for biomedical applications. Colloid Surf B 2008;64:111–7.
[21] Yang J, Lee T-I, Lee J, Lim E-K, Hyung W, Lee C-H, et al. Synthesis of ultrasensitive magnetic resonance contrast agents for cancer imaging using PEG-fatty acid. Chem Mater 2007;19:3870–6.
[22] Basu Ray G, Chakraborty I, Moulik SP. Pyrene absorption can be a convenient method for probing critical micellar concentration (cmc) and indexing micellar polarity. J Colloid Interface Sci 2006;294:248–54.
[23] Zhang JX, Qiu LY, Jin Y, Zhu KJ. Thermally responsive polymeric micelles self-assembled by amphiphilic polyphosphazene with poly(N-isopropylacrylamide) and ethyl glycinate as side groups: polymer synthesis, characterization, and in vitro drug release study. J Biomed Mater Res A 2006;76A(4):773–80.
[24] Michalet X, Pinaud FF, Bentolila LA, Tsay JM, Doose S, Li JJ, et al. Quantum dots for live cells, in vivo imaging, and diagnostics. Science 2005;307:538–44.
[25] Lim E-K, Yang J, Suh J-S, Huh Y-M, Haam S. Self-labeled magneto nanoprobes using tri-aminated polysorbate 80 for detection of human mesenchymal stem cells. J Mater Chem 2009;19:8958–63.
[26] Kamat AM, Karashima T, Davis DW, Lashinger L, Bar-Eli M, Millikan R, et al. The proteasome inhibitor bortezomib synergizes with gemcitabine to block the growth of human 253JB-V bladder tumors in vivo. Mol Cancer Ther 2004;3:279–90.
[27] Yang J, Lee C-H, Ko H-J, Suh J-S, Yoon H-G, Lee K, et al. Multifunctional magneto-polymeric nanohybrids for targeted detection and synergistic therapeutic effects on breast cancer13. Angew Chem Int Ed 2007;46:8836–9.
[28] Jeon SI, Lee JH, Andrade JD, De Gennes PG. Protein–surface interactions in the presence of polyethylene oxide: I. Simplified theory. J Colloid Interface Sci 1991;142:149–58.
[29] Valdes-Aguilera O, Pathak CP, Neckers DC. Pyrene as a fluorescent probe for monitoring polymerization rates. Macromolecules 1990;23:689–92.
[30] Tanaka T, Shiramoto S, Miyashita M, Fujishima Y, Kaneo Y. Tumor targeting based on the effect of enhanced permeability and retention (EPR) and the mechanism of receptor-mediated endocytosis (RME). Int J Pharmaceut 2004;277:39–61.
[31] Debatin JGF, Nadel SN, Paolini JF, Sostman HD, Coleman RE, Evans AJ, et al. Cardiac ejection fraction: phantom study comparing cine MR imaging, radionuclide blood pool imaging, and ventriculography. J Magn Reson Imaging 1992;2:135–42.
[32] Son YJ, Jang J-S, Cho YW, Chung H, Park R-W, Kwon IC, et al. Biodistribution and anti-tumor efficacy of doxorubicin loaded glycol-chitosan nanoaggregates by EPR effect. J Control Release 2003;91(1–2):135–45.